AGU
ADVANCING EARTH AND SPACE SCIENCES

JGR Oceans

Key Points:

- Foam area evolution from laboratory breaking waves and oceanic whitecaps is compared
- Self-similar behavior in foam area evolution is evident in laboratory and field data sets
- Energy dissipated by individual breaking waves can be estimated from foam area time history

Correspondence to:

A. H. Callaghan,
a.callaghan@imperial.ac.uk

Author Contributions:

Conceptualization: A. H. Callaghan, G. B. Deane, M. Dale Stokes
Data curation: A. H. Callaghan, G. B. Deane, M. Dale Stokes
Formal analysis: A. H. Callaghan
Funding acquisition: A. H. Callaghan, G. B. Deane, M. Dale Stokes
Investigation: A. H. Callaghan, G. B. Deane, M. Dale Stokes
Methodology: A. H. Callaghan, G. B. Deane, M. Dale Stokes
Project Administration: A. H. Callaghan
Resources: G. B. Deane, M. Dale Stokes
Validation: A. H. Callaghan
Writing – original draft: A. H. Callaghan
Writing – review & editing: G. B. Deane, M. Dale Stokes

A Comparison of Laboratory and Field Measurements of Whitecap Foam Evolution From Breaking Waves

A. H. Callaghan[1] , **G. B. Deane[2]** , and **M. Dale Stokes[2]**

[1]Department of Civil and Environmental Engineering, Imperial College London, London, UK, [2]Scripps Institution of Oceanography, La Jolla, CA, USA

Abstract Sufficiently energetic breaking ocean waves produce distinctive visible foam signatures on the water surface called whitecaps. The mixture of surface whitecap foam cells, and sub-surface bubbles, results in the broad-band scattering of light that allow whitecaps to be measured with optical cameras. In this paper the temporal evolution of whitecap foam area from laboratory and oceanic breaking waves is compared. When appropriately scaled, the foam area time series for both laboratory and oceanic breaking waves follow similar trends, despite occurring in vastly different settings. Distinct similarities of the signature of foam stabilization due to the presence of surfactants in the controlled laboratory experiments are also found in the field suggesting foam stabilization may be a means to remotely sense the presence/absence or concentration of surfactants in the ocean. In addition, probability density distributions of key whitecap variables such as foam area growth and decay timescales and maximum foam area are compared between laboratory and oceanic whitecaps. The oceanic whitecaps are much larger in scale than the laboratory breaking waves, whereas the whitecap growth and decay timescales are similar in magnitude, the latter suggesting that the depths to which bubbles are injected during active air entrainment in the field are relatively shallow. The aggregated whitecap statistics are used to estimate the energy dissipation of individual whitecaps in a novel manner.

Plain Language Summary The breaking of ocean waves is a key process controlling the evolution of oceanic sea states and the exchange of energy, momentum and material across the ocean-atmosphere interface. Despite their importance, little is known about the energetics of individual breaking waves in the ocean because of the difficulty in precisely measuring the complicated fluid motions they produce. However, when they are sufficiently energetic, they entrain air and appear as white foam patches on the water surface, and are called whitecaps. This means that their occurrence and scale can be measured using relatively affordable optical cameras. In this paper we show that the patterns of foam evolution in laboratory breaking waves and oceanic whitecaps are remarkably similar giving us confidence that what we learn from laboratory experiments can be confidently applied to real oceanic whitecaps. Building on this, we show what parts of the whitecap foam area evolution can be used to learn more about ocean chemistry and breaking wave energetics. We hope that further development of the principles outlined in this paper can transform how oceanic whitecaps are observed in the ocean and ultimately lead to a better understanding of ocean waves and their evolution.

1. Introduction

Breaking wind-generated gravity waves on the ocean surface that entrain sufficient amounts of air are seen as white patches and are called whitecaps (Monahan, 1986). The high volume of air entrained in these whitecaps, in the form of surface foam cells and subsurface bubbles, gives rise to the broadband scattering of light which results in their characteristic white appearance and associated high albedo (Frouin et al., 1996; Koepke, 1984). Whitecaps mark areas on the ocean surface where enhanced ocean-atmosphere exchange of energy, momentum and material occurs. Therefore, whitecaps play a fundamental role in ocean-atmosphere exchange and hence help to influence the evolution of weather and climate (Deike, 2021; Melville, 1996).

Much of what is known about the physics of breaking waves has been determined through careful laboratory experiments that have measured quantities such as energy dissipation and fluid turbulence, breaking speed and duration, Lagrangian mass transport, air entrainment, bubble plume depth, evolving foam area and the role of surfactants in foam stabilization (e.g., Callaghan et al., 2016; Cao et al., 2023; Deane et al., 2016; Deane & Stokes, 2002; Duncan, 1981; Lamarre & Melville, 1991; Lenain et al., 2019; Rapp & Melville, 1990; Sinnis et al., 2021; Tian et al., 2010). The laboratory experiments allow for: (a) the properties of incipient breaking

waves to be carefully controlled, (b) the precise placement of instrumentation to collect accurate measurements of surface and sub-surface flow properties, and (c) the careful manipulation of water chemistry. These kinds of detailed studies cannot be easily replicated in the field due to the associated practical difficulties.

In field studies, much of what has been learned about the occurrence of whitecaps has been achieved using a variety of remote sensing approaches such as using visible and infra-red cameras mounted in close proximity to the sea surface, radar, underwater passive acoustics and satellite-based sensors operating in the optical, near-infrared, shortwave infrared and microwave bands of the electromagnetic spectrum (e.g., Anguelova & Webster, 2006; Bondur & Sharkov, 1982; Callaghan et al., 2008; Ding & Farmer, 1994; Kubryakov et al., 2021; Malila et al., 2022; Melville & Matusov, 2002; Monahan, 1971; Phillips et al., 2001; Scanlon & Ward, 2016; Sutherland & Melville, 2013; Zou et al., 2022). Of the above-water remote sensing methods, the use of cameras provides the most convenient way to gather information on the spatial properties and statistics of individual whitecaps. The focus of this paper is to compare remote sensing measurements of individual surface whitecap characteristics made in the laboratory and the field using above-water optical cameras.

The seminal work of Duncan (1981) provided a framework in which to relate the phase speed of a quasi-steady laboratory breaking wave (c) to the rate of energy dissipated during the breaking process per unit breaking crest length (ϵ_l—[$W\,m^{-1}$]) following

$$\epsilon_l = b\rho g^{-1} c^5, \tag{1}$$

where b is the breaking strength parameter. Using Equation 1, estimates of ϵ_l for individual whitecaps could be made given measurements of c and an appropriate value of b. Remote sensing approaches are ideally suited to implement this approach in the field given the relative ease in which whitecaps can be identified in visible imagery of the sea surface. Furthermore, the work of Phillips (1985) provides a broader statistical framework in which the work of Duncan can be applied to populations of whitecaps. Indeed, the Duncan-Phillips framework has been used in studies of upper ocean turbulence, air-sea gas exchange and spectral wave modeling (Deike & Melville, 2018; Romero, 2019; Sutherland & Melville, 2013, 2015).

Notwithstanding these pioneering studies, the feasibility of the application of Equation 1 to estimate ϵ_l of individual whitecaps in the field has yet to be demonstrated due to challenges in constraining the value of b for individual whitecaps (Drazen et al., 2008). This is in contrast to laboratory studies in which b can be easily calculated and has been shown to be dependent on a measure of the slope of the breaking wave (Drazen et al., 2008). Field studies, therefore, have used the Duncan-Phillips framework to report average values of b, that is, b_{eff}, determined using an energy balance approach (Korinenko et al., 2020; Schwendeman et al., 2014; Zappa et al., 2016). While useful, this places limits on the depth of understanding on the variability of the energy dissipation of individual whitecaps that can be achieved. Alternative methods to estimate individual whitecap energy dissipation rates using remote sensing techniques are therefore needed.

One such alternative was presented by Callaghan et al. (2016), who outline a methodology developed in the laboratory, to estimate the total energy dissipated (and its rate) by individual breaking waves. The laboratory breaking waves were formed using dispersively focused wave groups in the absence of wind-forcing or currents. That study found that the volume of the sub-surface two-phase flow integrated in time when the surface whitecap foam area is increasing during the active wave breaking period scales linearly with the total energy dissipated by the breaking wave. No corresponding increase in the inferred space and time-averaged dissipation rate of turbulence in the water was found, consistent with the concept of fluid-turbulence saturation presented in Deane et al. (2016). The volume time-integral (VTI) model was applied to the data sets of Duncan (1981), Lamarre and Melville (1991) and Blenkinsopp and Chaplin (2007) and good agreement was found across all four studies. The implication is that measurements of the VTI for individual breaking waves can be used to estimate their energy dissipation. We note that Zou et al. (2022) have reported an underwater passive acoustic technique to estimate the breaking severity of individual whitecaps but we keep our focus in this paper to remote sensing techniques using above-water optical cameras.

The VTI for an individual breaking wave is expressed as

$$\Delta E_T = \Omega \rho A_o \hat{z}_p \tau_{growth} \tag{2}$$

where ΔE_T is the total energy in Joules dissipated, Ω is a turbulence strength parameter with a value of 0.88 W kg^{-1}, A_o is the maximum foam area of the whitecap, $\hat{z}_p$ is a foam area-weighted average bubble plume injection depth during active breaking and τ_{growth} is an integral timescale associated with the growth of the whitecap foam area

during active breaking. Callaghan et al. (2016) refer to $\hat{z}_p$ as a "penetration depth" and this terminology was used subsequently in Callaghan et al. (2017) and Callaghan (2018, 2020). Here, we replace the term "penetration depth" with "injection depth" to emphasize that $\hat{z}_p$ characterizes the average depth bubbles reach during active air entrainment. Of course, further turbulent motion can advect bubbles to larger depths over much longer timescales, and we note that bubbles generated by wave breaking have been found at depths in excess of 30 m (Strand et al., 2020). However, we maintain that bubbles are not injected to these depths during active wave breaking.

To apply Equation 2 to individual whitecaps in the field, all the variables that define the VTI need to be determined from surface whitecap foam characteristics. This is relatively straightforward for A_o and τ_{growth} which can be measured directly. However, $\hat{z}_p$ needs to be estimated from a characteristic whitecap area decay time, τ_{decay}, as shown in Callaghan et al. (2016). This approach can be complicated because the decay time for individual whitecaps can be influenced by the presence of surfactants which act to stabilize surface foam and lead to decay timescales larger than those expected in water free from surfactants. A methodology to identify, quantify and remove the effects of surfactant-driven foam stabilization in the decay time was presented and validated in Callaghan et al. (2017). While potentially very useful, the VTI approach has not yet been used to estimate distributions of energy dissipation for individual oceanic whitecaps.

Given the gap between the extensive measurements that are possible in the laboratory to constrain the energetics, surface and sub-surface properties of individual breaking waves compared to the more limited scope of field measurements, it is important to establish a set of measurements that can be made in the field which can apply what has been learned in laboratory experiments to oceanic whitecaps. Moreover, it is reasonable to ask the question "Are energy dissipation results derived from laboratory experiments on wave breaking directly applicable to whitecaps in the field?". This is a valid question because of the disparity in spatial and temporal scales between the breaking waves typically generated in the laboratory ($\mathcal{O}(1\ m)$ and $\mathcal{O}(1\ s)$), and oceanic whitecaps ($\mathcal{O}(10 - 100\ m)$ and $\mathcal{O}(1 - 10\ s)$). Additionally, while laboratory experiments can determine the energy dissipated by individual breaking waves directly, similar approaches cannot be easily applied in the field. Therefore, estimates of whitecap energy dissipation produced by using either the Duncan (1981) or Callaghan et al. (2016) approaches cannot yet be directly verified in the field by independent measurement at the scale of individual whitecaps. What can be done, however, is to establish whether or not patterns of behavior found in laboratory breaking waves are also found in oceanic whitecaps and to then conclude if this is sufficient to reasonably apply laboratory-derived results to field data.

The goal of this paper is to compare and contrast the foam area evolution of oceanic whitecaps to laboratory breaking waves and to apply the VTI method to a data set of 508 individual whitecaps to estimate their associated energy dissipation. It is beyond the scope of this paper to compare and contrast the breaking speed measurements in laboratory breaking waves and oceanic whitecaps needed to evaluate the Duncan (1981) method and the reader is directed to the work of Kleiss and Melville (2010); Kleiss and Melville (2011) and Schwendeman et al. (2014) for further reading. This paper proceeds as follows. Section 2 introduces the laboratory and oceanic breaking wave data sets along with the approach to calculate all relevant variables. Section 3 presents and discusses the results while final conclusions are given in Section 4.

2. Data Sets and Methodology

The data used here have been derived from measurements taken in both laboratory and field experiments. Full details of these experiments are provided in Callaghan et al. (2013, 2016) for the laboratory measurements and the field data are presented in Callaghan et al. (2012), and only the salient details are reproduced here.

2.1. Laboratory Experiments

The laboratory experiments were conducted in a wave channel in the Hydraulics Laboratory at the Scripps Institution of Oceanography in 2012 (Callaghan et al., 2013). Air-entraining breaking waves were generated in seawater using a dispersive focusing method that allowed the position of the breaking to be controlled in a deterministic and repeatable manner. The seawater was pumped from La Jolla Shores and filtered before filling the wave channel. Wire wave gauges placed upstream and downstream of the breaking region allowed the time-integrated energy flux along the channel to be calculated into and out of a control volume centered on the location of the breaking wave and the energy dissipated by each individual breaking wave to be calculated.

The breaking process was recorded by a pair of time-synchronised 1 mega pixel Red Lake Motion Pro X cameras at a frame rate of 30 frames per second: an overhead camera captured the evolution of the surface foam generated, and a side-viewing camera imaged the evolving sub-surface bubble plume. The water chemistry was altered through the addition of Triton X-100 in a concentration of 204 µg L^{-1} in order to mimic ocean conditions of medium productivity (Wurl et al., 2011). The purpose of adding Triton X-100 was to investigate any changes in foam lifetime at the water surface due to changes of the water's surface tension. For the purposes of description, the two experiments with different water types are referred to as "Filtered" and "Surfactant-Added."

By varying the slope of the wave groups a series of 30 breaking waves varying from gently spilling to strongly plunging were generated. The overall slope of each breaking wave group was altered via two different methods, described in detail in Section 2c of Callaghan et al. (2013) and these are termed Amplitude Modulation (AM) and Spectral Modulation (SM) methods. The Filtered experiments used both methods of wave modulation, whereas the Surfactant-Added experiments used the SM method only. By employing the AM and SM methods breaking waves groups with the same nominal slope but different inherent spectral bandwidths were generated. We refer the reader to (Callaghan et al., 2013) for more details.

2.2. Field Experiments

The field data were acquired during the Surface Processes and Acoustic Communication Experiment in 2008 (SPACE08) from the Air-Sea Interaction Tower at the Martha's Vineyard Coastal Observatory (MVCO) south of Martha's Vineyard on the east coast of the USA. A 5 megapixel Arecont Vision camera with 17.5 mm Schneider lens was mounted 23 m above the mean sea level at an angle of 59° from the nadir. Sea surface images were recorded at a variable rate of between three and six frames per second, and wave data were recorded by an ADCP mounted 1.5 km north of the location of the camera. Meteorological data were recorded onshore by an anemometer on the MVCO shore mast.

Individual whitecaps were identified in the sea surface images using a binary thresholding approach to separate whitecap foam from unbroken background water. The 508 whitecaps were manually tracked from their point of incipient breaking to the point where the foam patch could no longer be easily identified. This occurred when the foam patch dissipated, merged with another foam patch on the water surface or was advected out of the image footprint. The manual tracking process was labor-intensive but yielded a data set of high fideilty with each whitecap carefully inspected throughout its observed lifetime. This process is described in more detail in Section 2.3.

Sea surface images were analyzed for breaking waves during 4 time periods. Table 1 in Callaghan et al. (2012) outlines the sea state properties and average wind speed for each of the four periods with key values reproduced here. Period I and Period II were characterized by relatively steady wind speed and direction with average wind speeds of 11.4 and 8.2 m s^{-1}, and average wind directions from 31° and 340°, respectively. The sea state during Period I was mixed with a significant swell wave height ($H_{s,swell}$) of 0.63 m propagating from 156° and a significant wind-wave height ($H_{s,ww}$) of 0.44 m propagating from 125°. Period II was dominated by a decaying wind sea with $H_{s,ww} = 0.55$ m propagating from 226° while $H_{s,swell} = 0.13$ m propagating from 178°. Period III had a steady wind with an average speed of 5.7 m s^{-1} blowing from 70°. The sea state was swell-dominated with $H_{s,swell} = 0.94$ m propagating from 168°, with $H_{s,ww} = 0.29$ m propagating from 144°. Period IV directly followed Period III and was characterized by a rapid increase in average wind speed rising from 5.7 to 13.7 m s^{-1} and a change in the wind direction from 70° to 206° over a period of 1 hr. The sea state during Period IV was still swell-dominated as in Period III, but the wind-wave field was rapidly developing with $H_{s,ww}$ rising to 0.47 m, with little change in the direction of propagation.

2.3. Methodology

Figure 1 shows images taken of two laboratory breaking waves and an oceanic whitecap, along with their respective measured foam area time series. Panels a–e and f-j show a breaking wave generated in the Filtered and Surfactant-Added experiments, respectively, with panels k–o showing the oceanic whitecap. Corresponding foam area time series for these three breaking waves are shown in panels p, q and r, respectively.

In all cases, the foam area evolution is characterized by a rapid initial increase when the wave is actively breaking and entraining air beneath the water surface before decaying thereafter. The peak in foam area is denoted
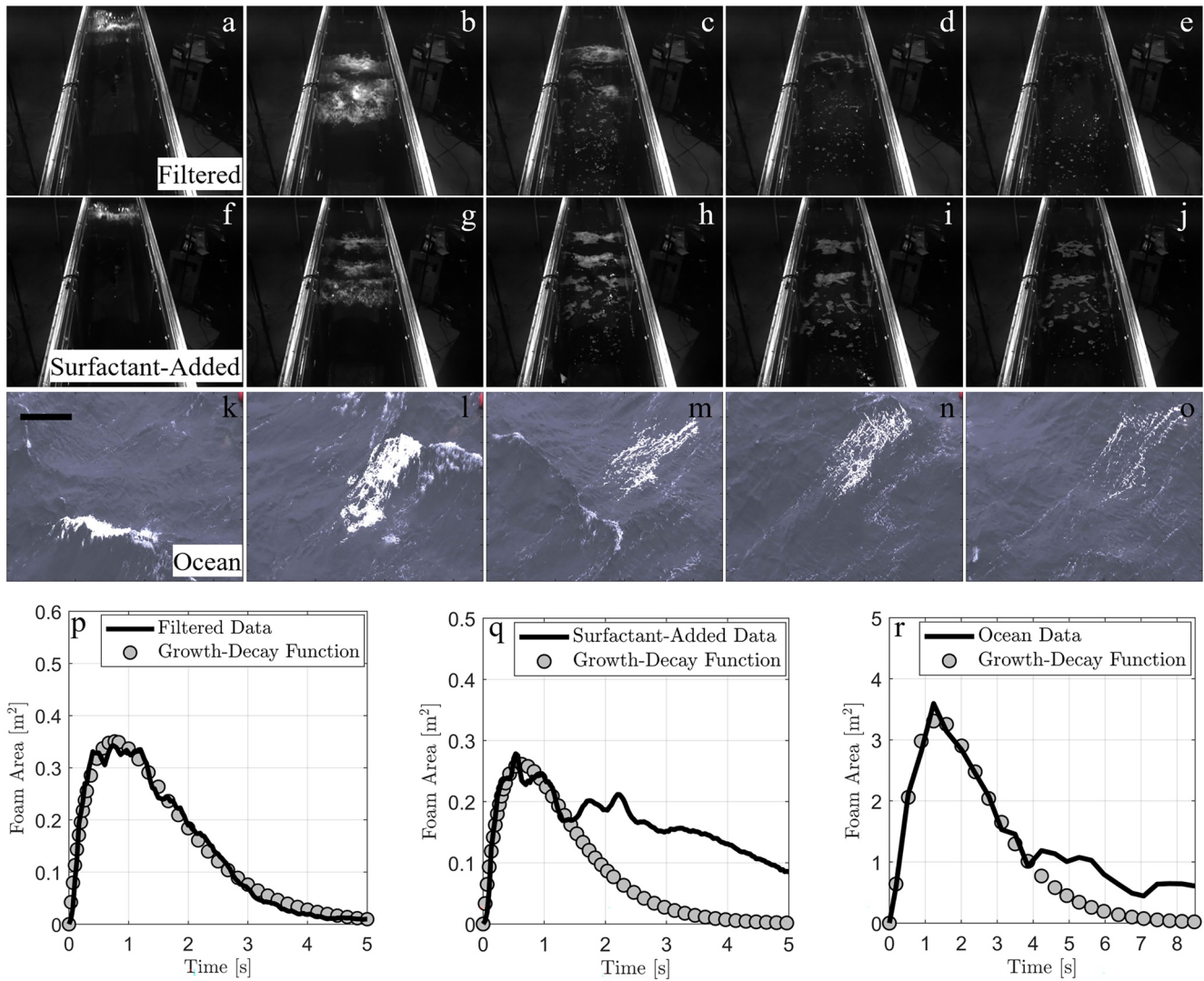
Figure 1. Panels (a–e) show the evolving whitecap foam from a breaking wave generated in the Filtered seawater experiment captured with the overhead camera. Panels (f–j) show a breaking wave generated in the Surfactant-Added seawater experiment. Panels (k–o) show a similar view of an oceanic whitecap from the field experiment where the horizontal black bar represents a scale of 1 m. The final three panels (p, q and r) show the corresponding measured foam area evolution (black line) for the Filtered and Surfactant-Added laboratory breaking waves and the oceanic whitecap, respectively. The closed gray circles correspond to the least mean squares fit of Equation 3.

as A_o, occurs at a time t_{A_o} and represents the time when foam area growth is balanced by foam area decay. The time t_{A_o} can be used to define a growth phase and a decay phase in the foam area evolution. In contrast to the growth phase, there is much more variability in the decay phase across all three examples shown. The decay phase is primarily controlled by two processes: bubble plume degassing and surfactant-driven foam stabilization (Callaghan et al., 2013; Masnadi et al., 2021). During the former, the surface whitecap is sustained as long as it is fed by a sufficient bubble flux from below. During the latter, the thin-film fluid drainage within the surface foam cells is reduced due to Marangoni forces arising from gradients in surface tension caused by variations in the surfactant loading on the foam cells (Henry, 2009). This causes the foam lifetime to increase over and above that expected in water free from surfactants.

Also shown in Figure 1p–1r is a growth-decay function of the form:

$$A(t) = c_o \, t^n \exp(-c_1 \, t) \tag{3}$$

where coefficients c_o, n and c_1 have been determined via a least mean squares fitting of equation 3 to the measured data. As discussed extensively in Callaghan et al. (2016, 2017) Equation 3 describes the foam area evolution

data very well for the Filtered laboratory experiments which had a film pressure of 1 mN m^{-1}. Film pressure is the difference in surface tension between surfactant-free water and a water sample and a value of 0 is expected for water free from surfactants. It is extremely difficult to completely remove surfactants from laboratory experiments at this scale, and therefore we consider the Filtered experiments to represent conditions when the effects of surfactant-driven foam stabilization are minimal.

The decay phase foam area evolution data shown in Figure 1q for a breaking wave generated in the Surfactant-Added experiment shows a markedly different behavior compared to that shown in Figure 1p from the Filtered experiment. The lower foam area rate of decay observed in the Surfactant-Added experiments is caused by an increase in film pressure to 4 mN m^{-1} from 1 mN m^{-1} after the addition of Triton X-100. As discussed in Callaghan et al. (2017), the effect of surfactant-driven foam stabilization is first reliably measureable at timescales of approximately $2t_{A_o}$. Until this point, the trend in the foam area evolution for the two breaking waves is similar. This observation gives a period of time $\left(\Delta t \approx 2t_{A_o}\right)$ over which Equation 3 can be fitted to the foam area evolution data from the Surfactant-Added experiments to approximate the expected evolution of the foam area in the absence of surfactant-driven foam stabilization. The result of this fitting procedure is shown in Figure 1q and the associated decay phase is taken to be representative of the contribution expected from bubble plume degassing only. The patterns displayed in Figure 1 panels p and q are representative of the laboratory data set.

The corresponding foam area evolution of the oceanic whitecap depicted in Figures 1k–1o is shown in Figure 1r. It shows very similar trends to the laboratory data shown in panels p and q. A distinct rapid increase in foam area is followed by a more gradual decay. Equation 3 is fitted to the measured data over a time period of 0–$2t_{A_o}$, in a manner similar to the laboratory data. The fit is interpreted to be the expected foam area evolution driven by air-entrainment and bubble plume degassing only. The difference between the fit and the data from a time of 4 s onwards is interpreted to be indicative of the effects of surfactant-driven foam stabilization.

2.4. Characteristic Foam Area Timescales

A variety of integral timescales to describe the foam evolution can be defined from the foam-area time series data. An integral growth timescale, τ_{growth}, can be calculated as $\tau_{growth} = A_o^{-1} \int_0^{t_{A_o}} A(t)dt$. If the growth phase were entirely linear, then $\tau_{growth} = 0.5t_{A_o}$ would be expected. Similarly, an integral decay timescale is calculated following $\tau_{decay} = A_o^{-1} \int_{t_{A_o}}^{\infty} A(t)dt$. Since the decay phase is controlled by both bubble plume degassing and surfactant-driven foam stabilization, it is useful to separate τ_{decay} into two components such that $\tau_{decay} = \tau_{degas} + \tau_{stab}$: τ_{degas} characterizes the timescale associated with bubble plume degassing only and τ_{stab} quantifies the additional time taken for the foam to decay in the presence of surfactants. τ_{degas} is calculated in the same way as τ_{decay} but using the fit of Equation 3 to the measured data as explained above. τ_{stab} is then simply calculated as $\tau_{stab} = \tau_{decay} - \tau_{degas}$.

Because of variability in the laboratory data, A_o and t_{A_o} are taken from the fit of Equation 3 to the data. This is reasonable given that the estimated error on the foam area measurements is $+16\%$ to -9% due to the assumption of a flat water surface (Callaghan et al., 2013). For the oceanic data, A_o and t_{A_o} are taken from the measurements.

3. Results and Discussion

The goal of the paper is to explore whether similarities between the foam area evolution of the laboratory breaking waves and the oceanic whitecaps can be established such that the understanding of the energy dissipation by laboratory breaking waves can be applied to oceanic whitecaps with confidence. Before doing so, it is useful to compare the measured foam area evolution curves for the entire data set comprising the laboratory breaking waves from the Filtered and Surfactant-Added experiments and the oceanic whitecaps from the field.

3.1. Raw Data

Panels a, b and c in Figure 2 show the measured foam area evolution for all the breaking waves from the Filtered experiments ($N = 20$), the Surfactant-Added seawater experiments ($N = 10$) and the SPACE08 field observations of oceanic whitecaps ($N = 508$), respectively. Figure 2 panels d, e and f show the same data but plotted with a logarithmic y-scale. Immediately obvious is the disparity in spatial scales between the laboratory data and the
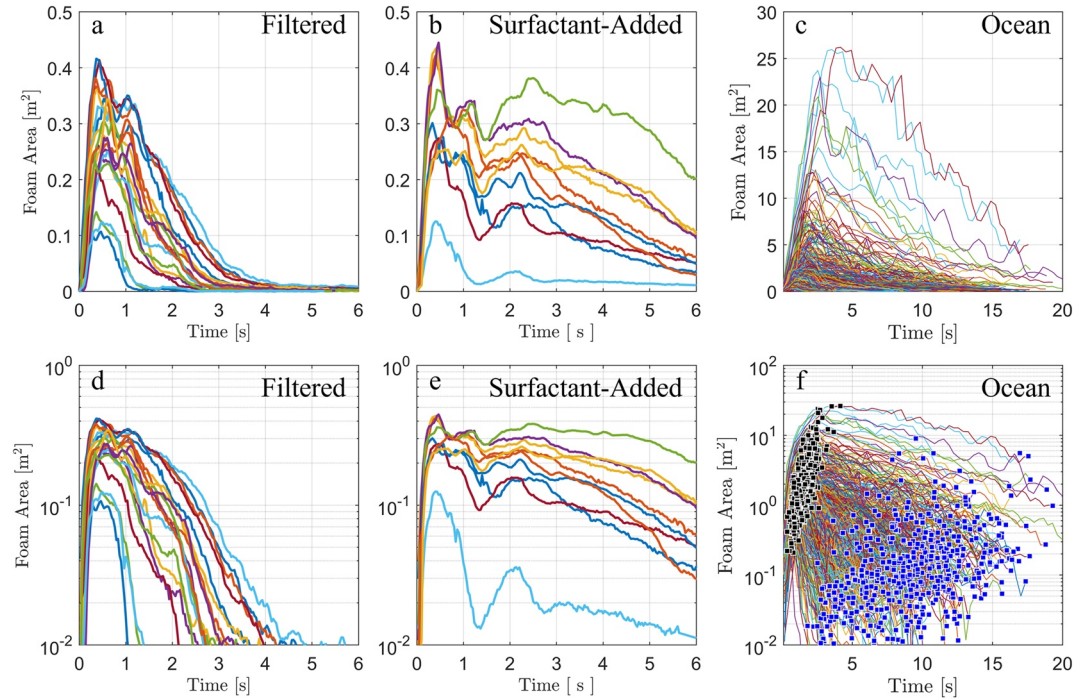
Figure 2. Panels (a, b, and c) display the foam area evolution for the breaking wave studied in the Filtered and Surfactant-Added laboratory experiments and oceanic whitecaps, respectively. Panels (d, e, and f) show the same data but with a logarithmic y-axis. The black and blue squares in panel (f) denote t_{A_o} and the last foam area measurement, respectively, for display purposes.

field data. The laboratory data are long-crested 2-dimensional waves whose width is constrained by the width of the wave channel and values of A_o range from 0.1 to 0.45 m^2. In contrast, the oceanic whitecaps A_o values range from 0.2 to 26 m^2, the latter being almost a factor of 30 larger in scale compared to the laboratory breaking waves. Total whitecap lifetimes for the laboratory data range from 1 to 5 s for the Filtered experiments increasing to 10 s for the longest lived foam patches in the Surfactant-Added experiments. The oceanic whitecap lifetimes encompass the range of lifetimes from the laboratory data extending from about 2 to 20 s.

3.2. Scaled Foam Area Data

Within the Filtered data set, the range of values of A_o and t_{A_o} varies by about a factor of 4 between the least and most energetic breaking wave. It is possible, however, to scale $A(t)$ such that all foam area time series follow a similar trend. Figure 3 shows all the foam area data from the Filtered experiments where $A(t)$ has been normalized by A_o (i.e., $A(t)/A_o$) and time has been normalized in a piecewise manner following:

$$
t_* = \begin{cases} \dfrac{t}{t_{A_o}}; & t \leq t_{A_o} \\[2ex] \left(\dfrac{t - t_{A_o}}{\tau_{degas}} \right) + 1; & t > t_{A_o} \end{cases} \tag{4}
$$

As seen in Equation 4, the growth phase time period is normalized by t_{A_o} while the decay phase is normalized by τ_{degas}. The former is representative of the breaking duration and the latter is representative of the time taken for the sub-surface bubble plume to degas which is expected to be closely related to the bubble plume injection depth (Callaghan et al., 2013). This dual scaling has the result of collapsing the foam area evolution data from all breaking waves as shown with a linear and logarithmic vertical axis in Figures 3a and 3b respectively. Figures 3c and 3d show the ensemble average of the same data in panels a and b, respectively, along with the ensemble average of the fitted form of Equation 3 to each individual breaking wave. The figures show that, with appropriate
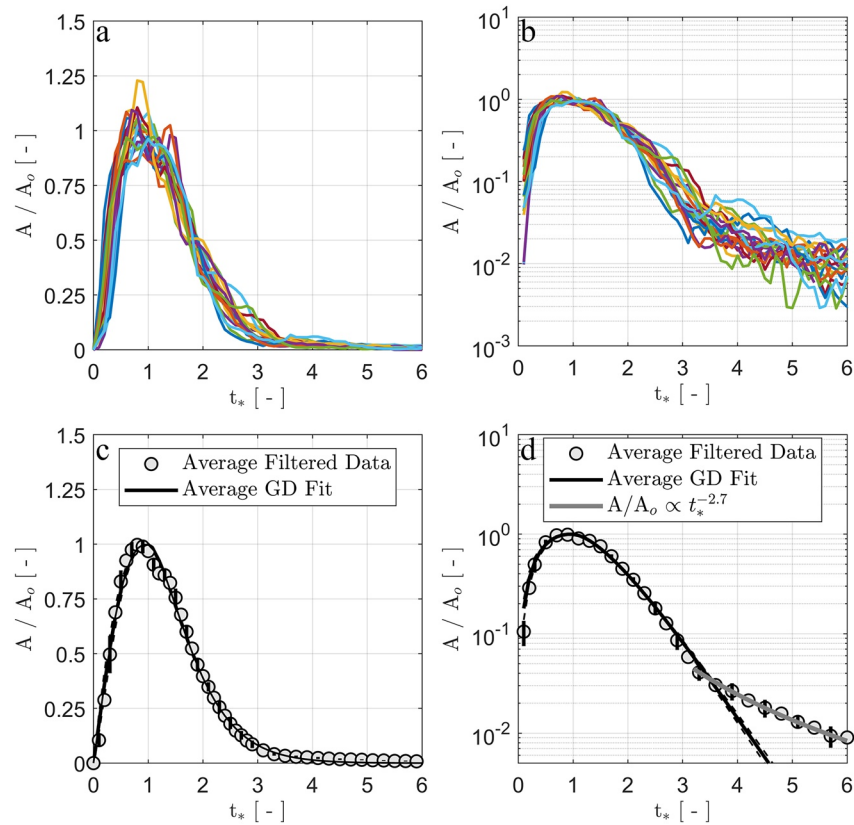
Figure 3. Normalized foam area evolution for the Filtered laboratory experiments. Panel (a) shows the scaled foam area evolution normalized following the procedure outlined in Section 3.2. Panel (b) is as panel (a) but with a logarithmic *y*-axis. The closed circles in panels (c) and (d) are the ensemble average of the data in panels (a) and (b), respectively. The solid black line is the ensemble average of Equation 3 fitted to each time series. The additional solid gray line in panel (d) is a power law fitted to the data at times $t_* > 3$ which indicates the influence of surfactant stabilization of the surface foam at very low values of A/A_o.

scaling, the foam area data display a self-similar behavior. This suggests that the foam area growth phase develops in a similar manner across the breaking waves studied here and that the degassing timescale is the most appropriate timescale to collapse the decay phase when surfactant-driven foam stabilization is not important. It should be pointed out that Callaghan et al. (2016) found that τ_{degas} followed a power law relationship with $\hat{z}_p$, such that $\hat{z}_p$ can be estimated from τ_{degas} determined with above water imagery. It is important to note that the normalized foam area data from the Filtered experiments diverge from Equation 3 for times $t_* > 3$ and display features associated with surfactant-driven foam stabilization. This is not surprising given the experimental conditions and that the measured film pressure was non-zero. In any case this signal occurs at a very low value of $A/A_o \approx 3\%$.

The same scaling procedure described above was applied to the breaking wave data collected in the Surfactant-Added experiments and is displayed in Figure 4. Similarly to the Filtered data, there is a self-similar behavior to the scaled data during the growth phase of foam evolution, and up to times of $t_* \approx 1.5$ into the decay phase. Thereafter, the effects of surfactant-driven foam stabilization cause the data to depart from the Filtered data and show much more variability. The implication is that the presence of surfactants does not appreciably affect the growth phase foam area evolution and the initial stage of the decay phase when bubble plume degassing is the dominant process affecting foam area decay. Once surfactant-driven foam stabilization becomes the dominant process in the decay phase, τ_{degas} cannot collapse the data. Also shown in Figures 4c and 4d is the ensemble average of all fits of Equation 3 to each foam area time series before surfactant-driven foam stabilization dominates the foam area decay phase. For comparison the ensemble average of the normalized data from the Filtered experiments is included in Figures 4c and 4d. The excellent agreement between the ensemble-averaged fit of Equation 3 to Filtered and Surfactant-Added data suggests that the expected foam area evolution in the absence of surfactant-driven foam stabilization can be well approximated even when the latter causes foam lifetimes to be extended.
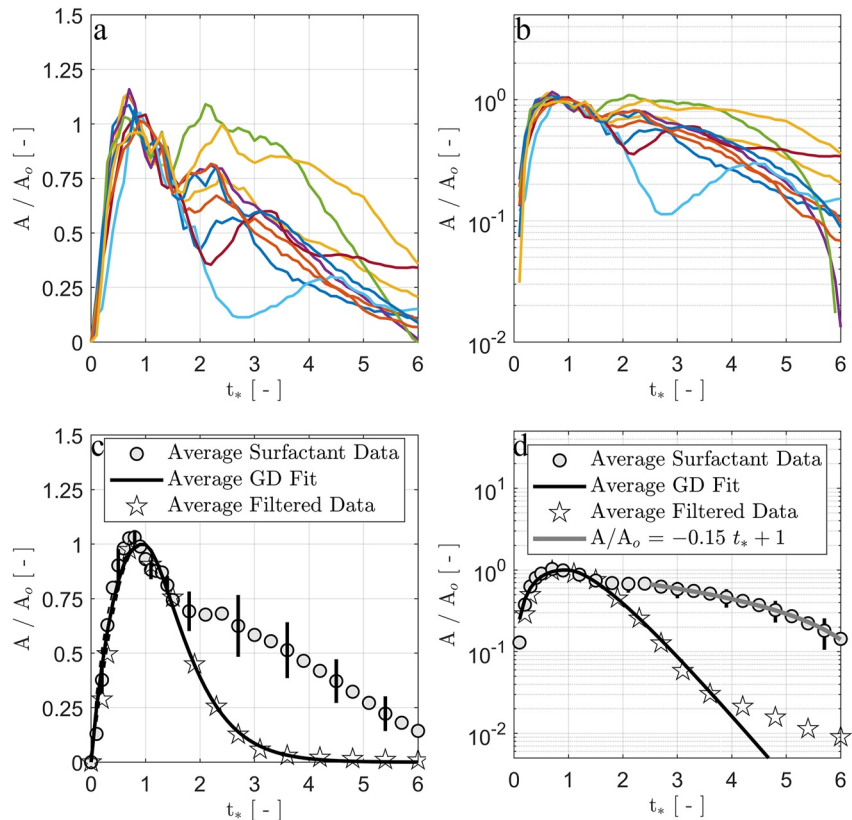
Figure 4. Normalized foam area evolution for the Surfactant-Added laboratory experiments. Panels (a) and (b) show the evolution of the scaled Surfactant-Added laboratory foam area data with a linear and logarithmic vertical axis, respectively. The closed gray circles in panels (c) and (d) depict the corresponding ensemble averages and the stars show the ensemble averaged data from the Filtered laboratory experiment for reference. The solid black curves in panels (c) and (d) represent the ensemble average of the fit of Equation 3 to the Surfactant-Added foam area data, as described in Section 3.2. Vertical black lines respresent ± 1 standard error.

Having identified the self-similar foam area evolution for the laboratory breaking waves, the same scaling procedure is now applied to the oceanic whitecap data with the results shown in Figure 5. Immediately apparent is that the upper and lower envelopes of the field data are captured remarkably well by the Surfactant-Added and Filtered laboratory data, respectively. This is a notable result given the scale difference between the two data sets. The implication is that the breaking process driving the foam area evolution in the laboratory and oceanic data sets is similar. Since foam area evolution is driven primarily by air entrainment, bubble plume degassing and surfactant-driven foam stabilization, it is reasonable to assume that these processes are similar in both the laboratory and field data sets. As stated above, the concentration of Triton X-100 used in the Surfactant-Added experiments was chosen to represent conditions of medium ocean productivity (Wurl et al., 2011) and it appears to capture the degree of foam stabilization observed in the field data very well.

Notwithstanding the overall similarities between the field and laboratory data in Figure 5, there are some noteworthy differences. For example, the laboratory data largely lie above the field data during the growth phase for $t_* < 1$ and are statistically significantly different, as quantified in table S1 and seen in figure S1 in the Supporting Information. This reflects the fact that the laboratory breaking waves can be considered to be 2-D unidirectional long-crested breakers, where as the oceanic whitecaps are 3-D short-crested breakers. For the former, breaking occurs at roughly the same time along the entire wave crest, whereas for the latter, the breaking is initiated over a relatively short segment of crest length and then spreads out laterally during the breaking process. The net effect is that the foam area increases more rapidly for the laboratory breakers compared to the oceanic whitecaps resulting in the differences in growth phase foam area evolution.

To compare the decay phase foam area evolution in more detail, Figure 6 categorizes the field data according to the foam stabilization factor, Θ, formulated in Callaghan et al. (2017). The parameter Θ quantifies the
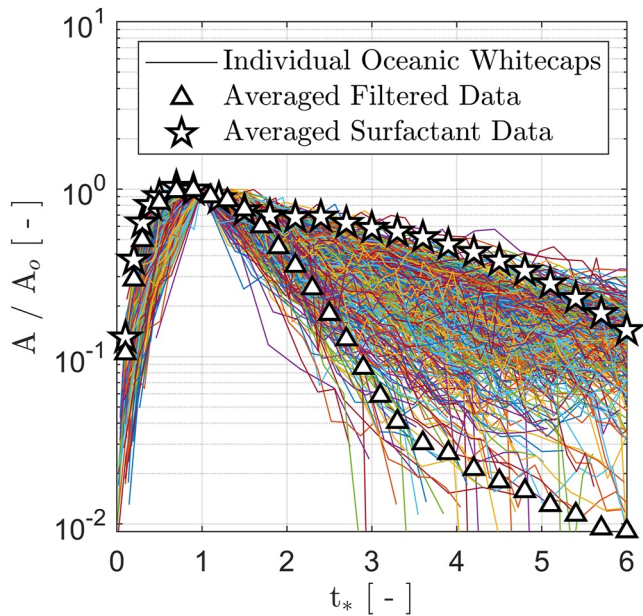
Figure 5. Colored lines represent the evolution of the scaled foam area time-series for all the oceanic whitecaps investigated here. The triangles and stars show the ensemble-averaged laboratory data from the Filtered and Surfactant-Added experiments, respectively, for comparison.

relative influence of bubble-plume degassing and surfactant-driven foam stabilization in controlling the whitecap decay phase. A value $\Theta = 1$ indicates bubble-plume degassing entirely controls the decay phase. As surfactant-driven foam stabilization becomes more important the value of Θ increases from 1. Four Θ bin-ranges are examined here ($1 \leq \Theta < 1.1$, $1.1 \leq \Theta < 1.5$, $1.5 \leq \Theta < 2$ and $\Theta \geq 2$) with the respective normalized foam area curves shown in Figures 6a–6d. The corresponding ensemble average values are shown in Figures 6e–6h and also in Figures 6i–6l but with logarithmic y-axis. Both of the averaged laboratory data sets are also shown for reference. As Θ increases, the measured field data depart from the Filtered data and approach the Surfactant-Added data. This departure occurs at earlier values of t_* as Θ increases and the rate of foam area decay also decreases. It is evident that the trends observed in the controlled laboratory experiments are also found in the oceanic whitecap data.

3.3. Comparison of Spatial and Temporal Scales

While there is an expected disparity in scale between the laboratory and field data as described in Section 3.1 and Section 3.2, appropriate normalization of the foam area time-series reveals a self-similar evolution within each data set and across the combined laboratory and field data sets. In this section we compare distributions of the laboratory and field data to learn more about their similarities and differences. A series of two-sample Kolmogorov-Smirnov statistical tests was carried out on the data sets to quantify the probability (p-value) that the data were drawn from different continuous distributions. The corresponding p-values are presented in the Supporting Information.

Figures 7a–7d compares probability density distributions of A_o, t_{A_o}, τ_{growth} and $\frac{t_{A_o}}{\tau_{growth}}$ from the laboratory and field data sets. As seen in Figure 7a, the spatial scales of the laboratory data overlap with the lower end of the field data, but the field data are up to two orders of magnitude greater than the laboratory data. Of note is the similar distributions in A_o for the laboratory data in Filtered and Surfactant-Added seawater indicating that the foam generation process in the two experiments was similar notwithstanding the differences in surfactant concentration. The distribution of A_o in the field data set shifts to larger values with increasing wind speed as could be expected. Period IV with the highest wind speed is the exception because, as discussed above, it was characterized by rapidly changing wind speed and direction. All corresponding p-values are shown in table S2.

Distributions of t_{A_o} and τ_{growth}, along with their ratio, are shown in Figures 7b–7d respectively with the corresponding p-values presented in Tables S3, S4, and S5 in Supporting Information S1. Values of t_{A_o} and τ_{growth} for the laboratory and field data are much closer when compared to the disparity in spatial scales but the corresponding p-values are <0.001. In terms of t_{A_o}, the field data are approximately twice those of the laboratory data indicating the oceanic whitecaps break for a longer duration than the smaller scale laboratory waves, which is most likely a reflection of the larger underlying wavelength of the oceanic whitecaps. Interestingly, a strong wind speed dependence on values of t_{A_o} and τ_{growth} is not seen unlike that for A_o, supported by the p-values in Tables S3 and S4 in Supporting Information S1. It is beyond the scope of this paper to explore the reasons why, and larger data sets would likely be needed.

The ratio $\frac{t_{A_o}}{\tau_{growth}}$ for the laboratory data is generally lower than the field data as seen in Figure 7d. This is to be expected since the laboratory breaking waves are unavoidably 2-dimensional which results in a faster rate of increase of foam area during the growth phase when compared to the 3-dimensional oceanic whitecaps, as explained in Section 3.2. This conclusion follows from the results presented in Figure 5 and is supported by the statistical results in Table S5 in Supporting Information S1.

Scatter plots of t_{A_o} and τ_{growth} with A_o for the combined data set are shown in Figures 8a and 8b, respectively. Notwithstanding the statistically significant differences in spatial and temporal scales between the laboratory and field data, Figures 8a and 8b indicates similar relationships between the timescales and maximum area for the laboratory and field data. Additionally, while the trend of τ_{growth} with A_o is similar between the laboratory and
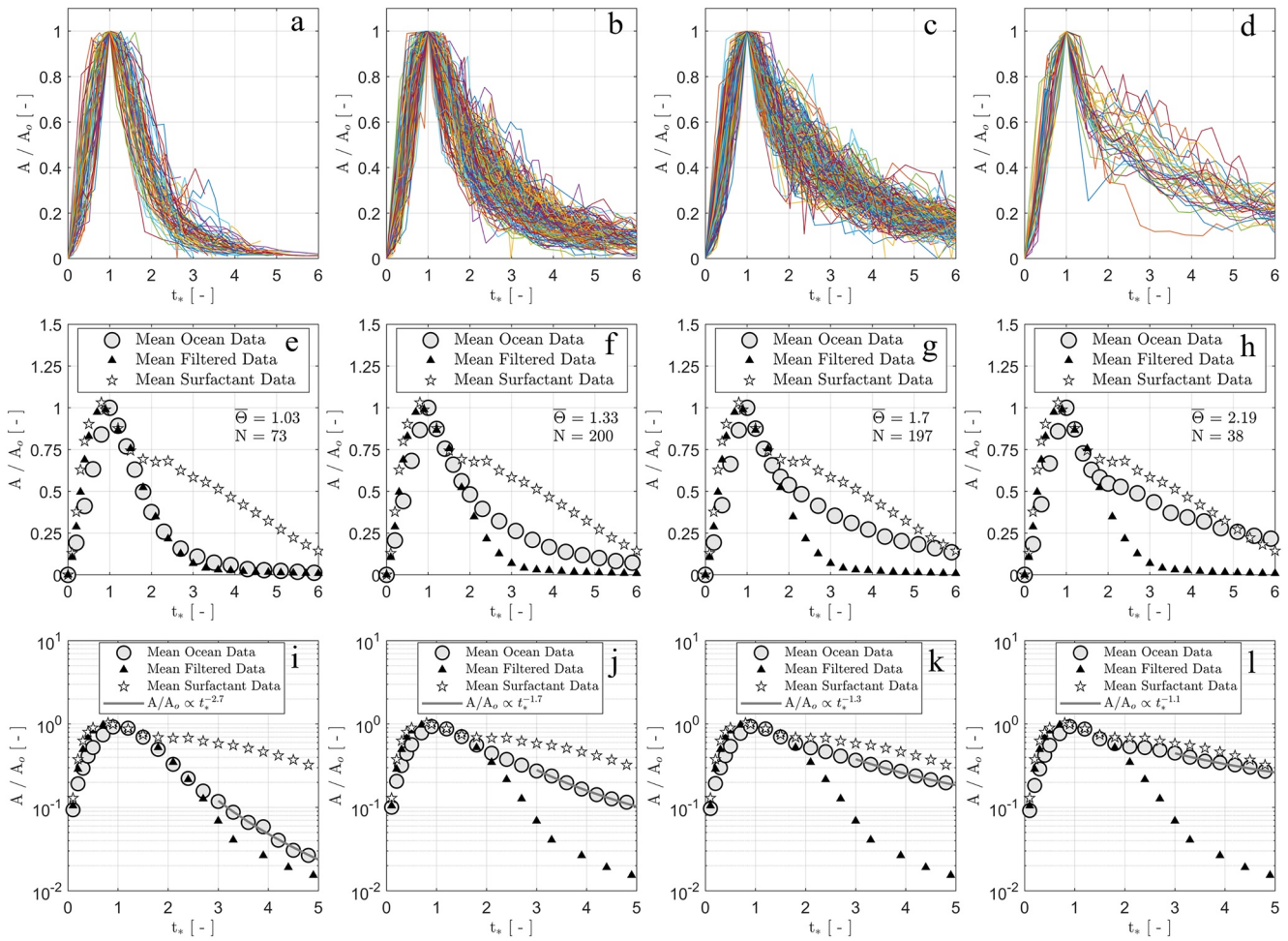
Figure 6. Panels (a–d) show the evolution of scaled foam area for the oceanic whitecaps with stabilization factor values that lie within the ranges $1 \leq \Theta < 1.1$, $1.1 \leq \Theta < 1.5$, $1.5 \leq \Theta < 2$ and $\Theta \geq 2$, respectively. Panels (e–h) and (i–j) show the ensemble average of the data in panels (a–d) on linear and logarithmic vertical axes, respectively. Also shown for reference in panels (e–l) are the ensemble averaged laboratory data from the Filtered (black triangles) and Surfactant-Added (open stars) experiments.

field data, the former lies toward the upper end, but within the scatter, of the field data. This again reflects the difference in dimensionality between the laboratory and field data as discussed above. Furthermore, the field data do not reveal systematic wind speed dependent differences in the relationship between the timescales and A_o data suggesting a similar breaking behavior across the environmental conditions sampled. It is interesting to note that the timescales and spatial scales presented in Figures 8a and 8b are up to two orders of magnitude larger than those presented in Figure 5e of Stringari et al. (2021). It is beyond the scope of this paper to explore the reasons why, but it may be related to differences in image processing methodology.

As discussed above, the decay timescale (τ_{decay}) is influenced by both bubble plume degassing and surfactant-driven foam stabilization, each of which can be quantified with the timescales τ_{degas} and τ_{stab}, respectively. Figures 9a–9c shows distributions of τ_{decay}, τ_{degas} and τ_{stab}, respectively, for the combined data set. Immediately obvious is the strong overlap in τ_{decay} for laboratory and field data. The agreement is particularly notable between the Filtered data and the field data from the lowest wind speed period. Figures 9b and 9c shows that the agreement is preserved for both τ_{degas} and τ_{stab} and supported statistically with results in Tables S6, S7 and S8 in Supporting Information S1.

When considering τ_{degas}, Callaghan et al. (2016, 2017) have shown that it can be used to estimate the value of the whitecap foam area-weighted bubble plume injection depth, $\hat{z}_p$. As can be seen in Figure 9b the measured laboratory and field values of τ_{degas} are very similar in magnitude. The implication is that if the relationship between τ_{degas} and $\hat{z}_p$ derived from the laboratory experiments is valid for oceanic whitecaps, then the bubble
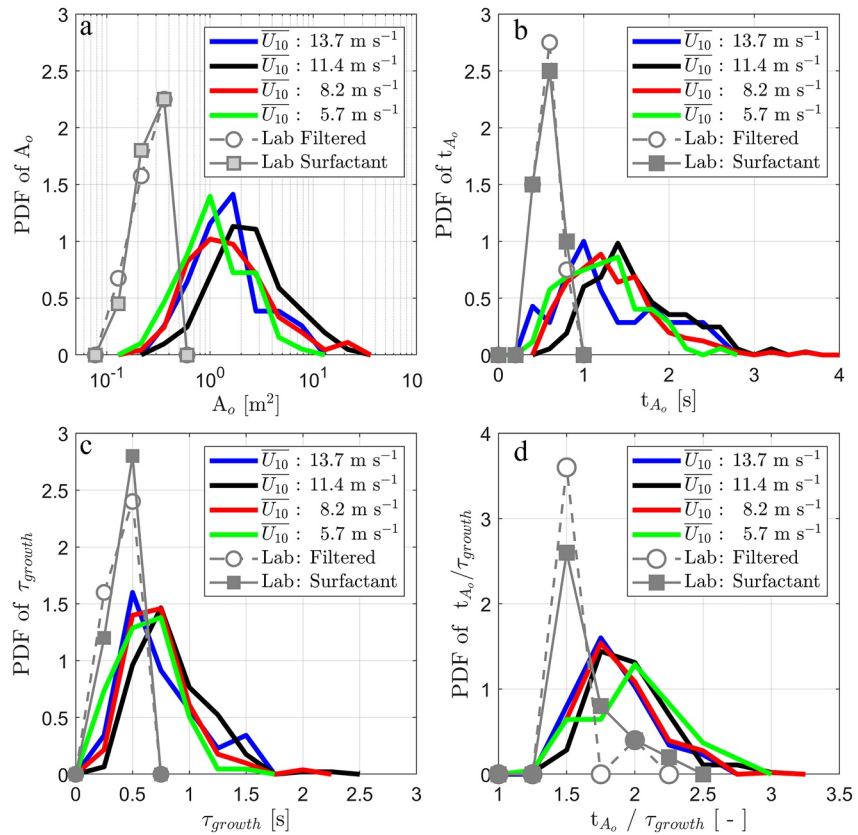
Figure 7. Panels (a–d) show the probability density distributions of the variables A_o, t_{A_o}, τ_{growth} and t_{A_o}/τ_{growth}, respectively. Colored lines represent field data while circles and squares represent the Filtered and Surfactant-Added laboratory data sets, respectively. Periods I, II, III and IV are represented by the black, red, green and blue lines, respectively.

plume injection depths associated with the laboratory and oceanic breaking waves are similar in magnitude, especially at low wind speeds. This is a notable result considering the order of magnitude differences in horizontal scale between the laboratory and field data. It supports the view that the bubble plume injection depth during active wave breaking is relatively shallow, being on the order of tens of centimeters rather than meters (Callaghan, 2018). Such a view is indirectly supported by the lack of observations of bubbles larger than a
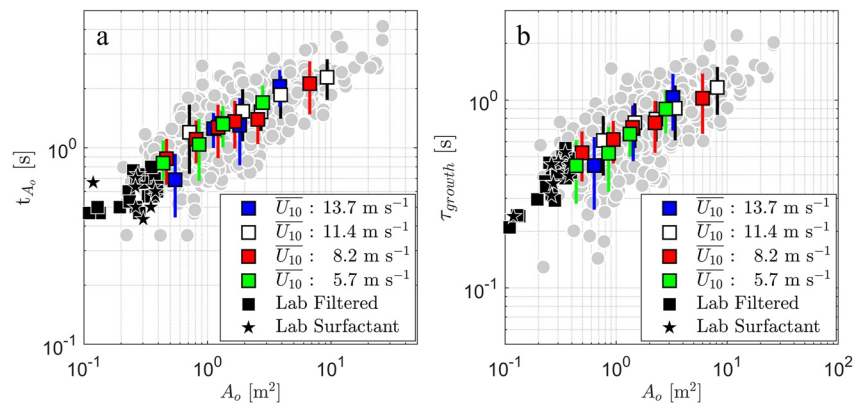

Figure 8. Panels (a and b) show the relationship of A_o with t_{A_o} and τ_{growth}, respectively, for the field and laboratory data sets. The gray circles are datapoints from all observation periods. Black squared and stars represent the Filtered and Surfactant-Added laboratory data respectively, while filled colored squares represent bin averaged field values for different observational periods. Periods I, II, III and IV are represented by the black, red, green and blue symbols, respectively. Vertical lines show ± one standard error on the bin averages.
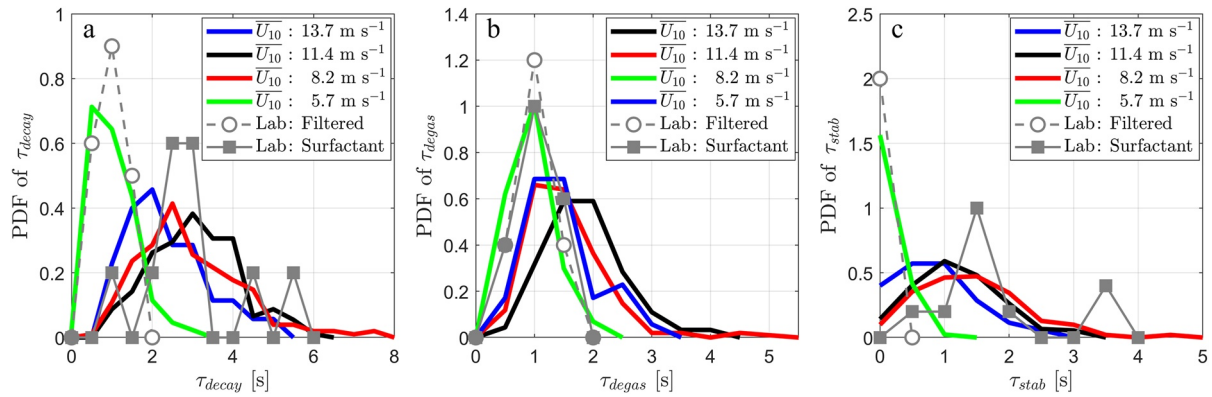
Figure 9. Panels (a–c) show the distributions of τ_{decay}, τ_{degas} and τ_{stab}, respectively, for the laboratory and field data sets. Different field observational time periods are color-coded and a distinction is made between the Filtered and Surfactant-Added laboratory data sets is made. Periods I, II, III and IV are represented by the black, red, green and blue lines, respectively.

few hundred μm, which are characteristically found inside actively breaking laboratory wave crests and oceanic whitecaps (see Deane and Stokes (2002)), within the upper 1–2 m of the water column even at wind speeds that exceed 20 m s^{-1} (Czerski et al., 2022a, 2022b). Concurrent measurements of τ_{degas} and $\hat{z}_p$ to evaluate the laboratory relationship in the field have yet to be made.

The distribution of τ_{stab} for the field and laboratory data show a strong degree of overlap. This is perhaps not that surprising as the concentration of TX-100 used in the Surfactant-Added experiments was chosen to mimic conditions of medium ocean productivity (Wurl et al., 2011). Indeed, the average value of the stabilization factor for the field data was 1.50 ($\pm$0.25), 1.66 ($\pm$0.30), 1.09 ($\pm$0.11) and 1.49 ($\pm$0.33) for Periods I, II, III and IV, respectively, compared to 1.02 and 2.28 for the Filtered and Surfactant-Added laboratory experiments, respectively (Callaghan et al., 2017).

Scatter plots of τ_{decay}, τ_{degas} and τ_{stab} with A_o are shown in Figures 10a–10c, respectively. Firstly, the figures clearly show that larger values of τ_{decay} for the Surfactant-Added seawater experiments are due to the large values of τ_{stab}, as noted above. For the Filtered data, the relationship between τ_{decay} and A_o follows the binned field data remarkably well, albeit occurring at smaller scales. However, when the effects of surfactants are removed and τ_{degas} is considered alone, it can be seen that while the trend in the combined laboratory data sets with A_o is similar to the bin-averaged oceanic data, they are shifted upwards compared to the field data. If a similar relationship between τ_{degas} and bubble plume injection depth exists in the field as was found in the laboratory (Callaghan et al., 2016), then Figure 10b implies that the bubble plumes formed under unforced dispersively focused laboratory breaking
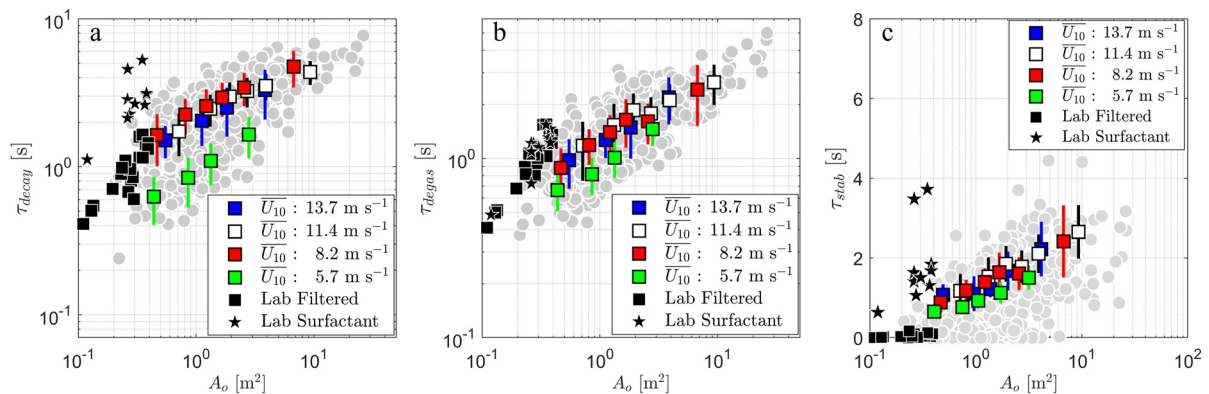

Figure 10. Panels (a–c) show the relationship of A_o with τ_{decay}, τ_{degas} and τ_{stab}, respectively, for the field and laboratory data sets. The gray circles are datapoints from all observation periods. Black squares and stars represent the Filtered and Surfactant-Added laboratory data respectively, while filled colored squares represent bin averaged field values for different observational periods. Periods I, II, III and IV are represented by the black, red, green and blue symbols, respectively. Vertical lines show $\pm$ one standard error on the bin averages.
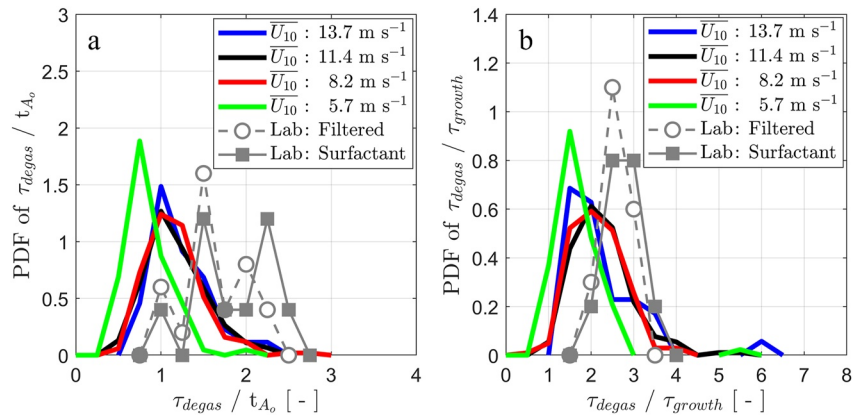
Figure 11. Panels (a) and (b) show the distributions of $\tau_{degas}/\tau_{growth}$, and τ_{degas}/t_{A_o}, respectively, for the laboratory and field data sets. Different field observational time periods are color-coded and a distinction is made between the Filtered and Surfactant-Added laboratory data sets is made. Periods I, II, III and IV are represented by the black, red, green and blue lines, respectively.

waves are relatively deeper than those formed underneath wind-forced oceanic whitecaps. We do not have the detailed measurements to confirm this, but our collective (unpublished) observations of laboratory breaking waves under direct wind forcing in wind-wave channels of different scales support this hypothesis.

The hypothesis that air is injected to deeper depths under the unforced laboratory breaking waves relative to the forced oceanic whitecaps is explored further in Figures 11a and 11b. Panels a and b, respectively, show that the peak of the ratios $\frac{\tau_{degas}}{\tau_{growth}}$ and $\frac{\tau_{degas}}{t_{A_o}}$ for the laboratory data lie at higher values when compared to the field data. The probability that the laboratory and field values of $\frac{\tau_{degas}}{\tau_{growth}}$ and $\frac{\tau_{degas}}{t_{A_o}}$ are drawn from the same distribution is small (see Tables S9 and S10 in Supporting Information S1). This suggests there may be some differences between how air is entrained in the laboratory and field breaking waves, possibly related to the interaction of the disintegrating wave crest and the unbroken water below. For example, in deep water wave breaking, it is often assumed that breaking waves can be described as either spilling or plunging. The former represent breaking waves where the disintegrating wave crest tumbles forward down the front face of the wave, while the latter implies an overturning jet is formed at the wave crest that reconnects with the water surface on the front face of the underlying wave entrapping a cylindrical tube of air. It is widely held that spilling breakers are the predominant type of breaking wave in deep water, and that dispersively focused waves are more plunging in nature. The data presented in Figures 11a and 11b, tend to support this qualitative distinction with the dispersive focused breaking laboratory breaking waves generating relatively deeper bubble plumes as indicated by Figures 11a and 11b.

3.4. Oceanic Whitecap Energy Dissipation

The preceding discussion in Section 3.2 has shown that when appropriately scaled, the foam area evolution for the laboratory breaking waves and the oceanic whitecaps exhibits remarkably similar behavior. It is our contention therefore that despite the differences in scale between the field and laboratory data sets described in Section 3.3, there is compelling and sufficient evidence that the volume-time integral model of Callaghan et al. (2016), validated with laboratory measurements, can be reasonably applied to individual oceanic whitecaps to infer their energy dissipation.

Figures 12a–12c shows distributions of the total energy dissipated (ΔE_T), the dissipation rate per unit breaking crest length ($\epsilon_l = \Delta E_T/\left(\overline{L} t_{A_o}\right)$) and the dissipation rate per unit whitecap area ($\epsilon_A = \Delta E_T/(A_o \tau_{growth})$), respectively, for the laboratory and field data sets. As with Figure 7a, immediately obvious is that the smaller laboratory breaking waves dissipate much less total energy than the larger scale oceanic whitecaps (see Table S11 in Supporting Information S1). Moreover, the peak in the distribution for the oceanic whitecaps shifts to larger values with increasing wind speed, as can be reasonably expected (the exception to this is for largest wind speed value of Period IV during which the wind was rapidly accelerating). This trend reflects the corresponding increase in A_o shown in 7(a) and, to a lesser extent, bubble plume injection depth as inferred from τ_{degas} in Figure 9b. It is important to note that the probability that ΔE_T from the Filtered and Surfactant-Added experiments are from the same continuous distribution approaches 1, as quantified in table S11 in the Supporting Information. Moreover, Figure
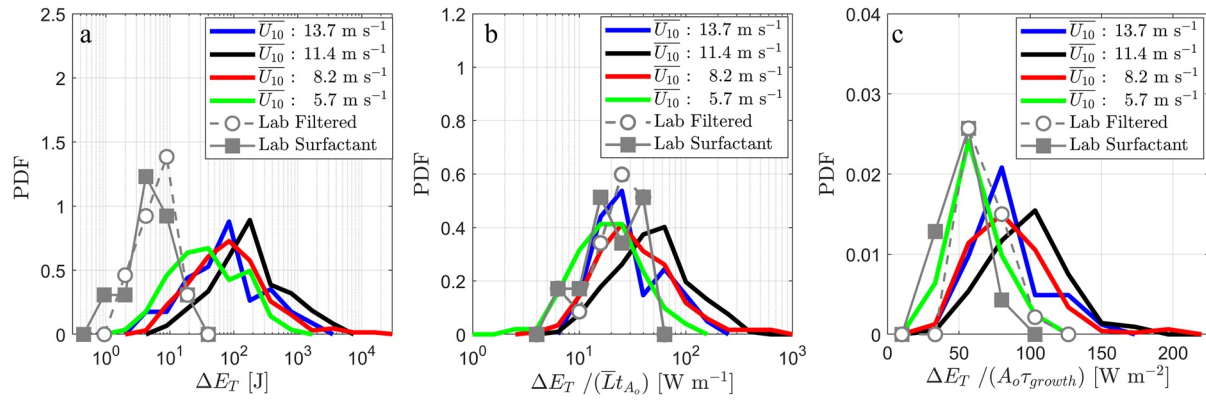
Figure 12. Panels (a–c) show the distribution of total energy dissipated (ΔE_T), the dissipation rate per unit breaking crest length ($\Delta E_T / \left(\overline{L} t_{A_o} \right)$) and the dissipation rate per unit whitecap area ($\Delta E_T/(A_o \tau_{growth})$), respectively, for the laboratory and field data sets. Periods I, II, III and IV are represented by the black, red, green and blue lines, respectively.

S2 in Supporting Information S1 confirms that the measured ΔE_T values from the two laboratory data sets follow the same trend with the volume time-integral as described in Callaghan et al. (2016).

In contrast to Figure 12a, the data in Figure 12b show a remarkable convergence in values of ϵ_l between the laboratory and field data sets, with the exception of Period I which is the observational period which had the highest steady wind speed at $\overline{U}_{10} = 11.4 \ m \ s^{-1}$. Whereas the absolute values of ΔE_T span up to four orders of magnitude, the majority of the ϵ_l values are spread across one order of magnitude. The statistical similarity in ϵ_l between the laboratory and field data sets is quantified in Table S12 in Supporting Information S1. The increase in p-values between the laboratory and field data sets for ϵ_l in Table S12 in Supporting Information S1, compared to ΔE_T in Table S11 in Supporting Information S1, suggests a certain degree of similarity in the breaking process in the laboratory and field data sets.

Figure 12c compares the energy dissipation rate per unit whitecap area, ϵ_A, for the laboratory and oceanic data sets. There is a further reduction in the range of values of ϵ_A compared to both ΔE_T and ϵ_l, discussed previously. Indeed, there is a remarkable similarity between the laboratory data and the Period III oceanic data set which had the lowest wind speed. The implication is that the bubble plume injection depths for Period III are most similar in magnitude to those in the unforced laboratory breaking waves.

The result of the statistical analysis in Table S13 in Supporting Information S1 which quantifies the similarity in ϵ_A values for the laboratory and field data sets presents an intriguing result. That is, the probability that the values of ϵ_A for the SM breaking wave groups in the Filtered and Surfactant-Added laboratory experiments and the field data from Period III are drawn from the same continuous distribution is $\approx 96\%$ and $\approx 30\%$, respectively, which is much higher than the other field observational periods. Interestingly, this probability falls to $< 1\%$ for the Filtered AM laboratory data set. As explained in Callaghan et al. (2013) and stated in Section 2.1 above, the wave group slopes of the breaking waves were modified using the AM and SM methods which resulted in different bandwidths for breaking waves with the same nominal wave group slope. Only the SM breaking wave groups were used in the Surfactant-Added experiment. We therefore speculate that bandwidth is an additional important factor that influences ϵ_A for individual breaking waves that have a similar wave group slope. From the data presented in Table S12 in Supporting Information S1 for ϵ_l, no clear bandwidth effect is evident. Indeed, the recent work of Cao et al. (2023) explicitly show that the fractional energy loss in laboratory breaking waves is bandwidth dependent, but that this bandwidth dependence greatly diminishes when considering the energy dissipation rate per unit crest length. Cao et al. (2023) did not explicitly examine the effect of bandwidth on ϵ_A.

4. Summary and Conclusions

A comparison of the temporal evolution of whitecap foam area for individual unforced laboratory breaking waves and wind-forced oceanic whitecaps using above-water digital image-based remote sensing has been presented. The motivation for doing so is threefold: (a) to explore the existence of similar behavior of foam area evolution within, and between, the laboratory and oceanic data sets, (b) to compare whitecap spatial and temporal scales of laboratory and field breaking waves and (c) to ascertain whether the volume time-integral method described in

Callaghan et al. (2016) and validated in the laboratory can be reasonably used to estimate the energy dissipated by individual whitecaps in the field. The latter point is of paramount importance because no routine estimates of energy dissipation of individual whitecaps in the field using above water imagery have been made despite much progress in laboratory experiments.

When appropriately scaled, foam area evolution for both laboratory whitecaps and field data show remarkable similarity during the foam area growth phase and also during the initial stages of foam decay, despite order of magnitude differences in scale. When bubble plume degassing is the dominant process controlling foam area decay, the scaled laboratory data collapse throughout the lifetime of the whitecaps until foam area has decreased to approximately 3% of its maximum value. Moreover, when the role of surfactant-driven foam stabilization is controlled for in the field data, a strikingly similar collapse is observed. When surfactant-driven foam stabilization is important its impact can be quantified via the stabilization factor presented in Callaghan et al. (2017).

Although largely similar, differences in the scaled whitecap area evolution during the growth phase between the laboratory and field data reflect differences related to the dimensionality of the breaking waves. The foam area increases more rapidly in the 2-dimensional, long-crested, unidirectional laboratory breaking waves compared to the 3-dimensional, short-crested, directionally spread oceanic whitecaps. This reflects the fact that breaking is nominally initiated uniformly along the entire wave crest in the 2-dimensional laboratory breaking waves, whereas in the 3-dimensional oceanic breaking waves, breaking is initiated over a confined portion of the steep wave crest and subsequently spreads laterally along the crest as breaking evolves.

A comparison of the foam area evolution between the laboratory and field breaking waves suggests that, for a given maximum foam area, the bubble plume injection depth is larger for unforced dispersively focused laboratory breaking waves than wind-forced oceanic breaking waves. This conclusion is reached by comparing the relationship of the bubble plume degassing timescale with maximum foam area, where the former can be considered proportional to bubble plume injection depth (Callaghan et al., 2016). Furthermore the ratio of τ_{degas} to both τ_{growth} and t_{A_o} also suggests that the bubble plume injection depth is deeper under dispersively focused laboratory breaking waves than under oceanic whitecaps.

The overwhelming similarity in scaled foam area evolution between the small scale laboratory breaking waves and full scale oceanic whitecaps supports the view that in many aspects dispersively focused laboratory breaking waves are a reasonable physical model for oceanic whitecaps, notwithstanding the potential discrepancies related to bubble plume injection depths summarized above. Consequently, we have assumed that the volume time-integral method of Callaghan et al. (2016) can be used to estimate the energy dissipated by individual oceanic whitecaps. Doing so, to the best of our knowledge, has produced the first reported distributions of breaking wave energy dissipated by individual oceanic whitecaps. The distributions reveal that in terms of absolute values, oceanic whitecaps dissipate much more energy than laboratory breaking waves due to the disparity in horizontal scale. However, this disparity is much reduced when the dissipation rate per unit crest length and per unit area are considered. Furthermore, the statistical analysis presented in the Supporting Information suggests that the dissipation rate per unit area may exhibit a bandwidth dependence, but more data are needed to examine this further.

To conclude, detailed laboratory breaking wave experiments provide the most comprehensive knowledge of the physics of wave breaking due to the relative ease of generation and measurement. The similarities in foam area evolution between the limited set of laboratory breaking waves and oceanic whitecaps presented here suggest that foam area evolution can be used to estimate energy dissipated by individual oceanic whitecaps. This is an important finding that can pave the way for routine estimates of breaking wave energy dissipation using above-water remote sensing of the sea surface. We acknowledge that the field data set presented here is limited in size due to the manual nature of analysis. The development of automated image processing routines that can identify and track individual whitecaps through their lifetime is needed to generate much larger data sets of oceanic whitecap energy dissipation. These larger data sets are necessary to further assess the application of the laboratory-derived volume time-integral to oceanic whitecaps in additional to complementary modeling studies.

Data Availability Statement

References

Anguelova, M. D., & Webster, F. (2006). Whitecap coverage from satellite measurements: A first step toward modeling the variability of oceanic whitecaps. *Journal of Geophysical Research*, *111*(3). https://doi.org/10.1029/2005JC003158

Blenkinsopp, C. E., & Chaplin, J. R. (2007). Void fraction measurements in breaking waves. *Proceedings of the Royal Society A: Mathematical, Physical and Engineering Sciences*, *463*(2088), 3151–3170. https://doi.org/10.1098/rspa.2007.1901

Bondur, V. G., & Sharkov, E. A. (1982). Statistical properties of whitecaps on a rough sea. *Oceanology*, *22*(3).

Callaghan, A. H. (2018). On the relationship between the energy dissipation rate of surface-breaking waves and oceanic whitecap coverage. *Journal of Physical Oceanography*, *48*(11), 2609–2626. https://doi.org/10.1175/JPO-D-17-0124.1

Callaghan, A. H. (2020). Estimates of wave breaking energy dissipation rate from measurements of whitecap coverage. In *Recent advances in the study of oceanic whitecaps* (pp. 25–41). Springer International Publishing. https://doi.org/10.1007/978-3-030-36371-0_3

Callaghan, A. H., Deane, G. B., & Stokes, M. D. (2013). Two regimes of laboratory whitecap foam decay: Bubble-plume controlled and surfactant stabilized. *Journal of Physical Oceanography*, *43*(6), 1114–1126. https://doi.org/10.1175/JPO-D-12-0148.1

Callaghan, A. H., Deane, G. B., & Stokes, M. D. (2016). Laboratory air-entraining breaking waves: Imaging visible foam signatures to estimate energy dissipation. *Geophysical Research Letters*, *43*(21), 11320–11328. https://doi.org/10.1002/2016GL071226

Callaghan, A. H., Deane, G. B., & Stokes, M. D. (2017). On the imprint of surfactant-driven stabilization of laboratory breaking wave foam with comparison to oceanic whitecaps. *Journal of Geophysical Research: Oceans*, *122*(8), 6110–6128. https://doi.org/10.1002/2017JC012809

Callaghan, A. H., Deane, G. B., & Stokes, M. D. (2023). A comparison of laboratory and field measurements of whitecap foam evolution from breaking waves [Dataset]. Figshare. https://doi.org/10.6084/m9.figshare.24534922.v2

Callaghan, A. H., Deane, G. B., Stokes, M. D., & Ward, B. (2012). Observed variation in the decay time of oceanic whitecap foam. *Journal of Geophysical Research*, *117*(9), 1–20. https://doi.org/10.1029/2012JC008147

Callaghan, A. H., de Leeuw, G., Cohen, L., & O'Dowd, C. D. (2008). Relationship of oceanic whitecap coverage to wind speed and wind history. *Geophysical Research Letters*, *35*(23), L23609. https://doi.org/10.1029/2008GL036165

Cao, R., Padilla, E. M., & Callaghan, A. H. (2023). The influence of bandwidth on the energetics of intermediate to deep water laboratory breaking waves. *Journal of Fluid Mechanics*, *971*, 1–28. https://doi.org/10.1017/jfm.2023.645

Czerski, H., Brooks, I. M., Gunn, S., Pascal, R., Matei, A., & Blomquist, B. (2022a). Ocean bubbles under high wind conditions - Part 2: Bubble size distributions and implications for models of bubble dynamics. *Ocean Science*, *18*(3), 587–608. https://doi.org/10.5194/os-18-587-2022

Czerski, H., Brooks, I. M., Gunn, S., Pascal, R., Matei, A., & Blomquist, B. (2022b). Ocean bubbles under high wind conditions – Part 1: Bubble distribution and development. *Ocean Science*, *18*(3), 565–586. https://doi.org/10.5194/os-18-565-2022

Deane, G. B., & Stokes, M. D. (2002). Scale dependence of bubble creation mechanisms in breaking waves. *Nature*, *418*(6900), 839–844. https://doi.org/10.1038/nature00967

Deane, G. B., Stokes, M. D., & Callaghan, A. H. (2016). The saturation of fluid turbulence in breaking laboratory waves and implications for whitecaps. *Journal of Physical Oceanography*, *46*(3), 975–992. https://doi.org/10.1175/JPO-D-14-0187.1

Deike, L. (2021). Mass transfer at the oceanocean-atmosphere interface: The role of wave breaking, droplets, and bubbles. *Annual Review of Fluid Mechanics*, *54*(1), 191–224. https://doi.org/10.1146/annurev-fluid-030121-014132

Deike, L., & Melville, W. K. (2018). Gas transfer by breaking waves. *Geophysical Research Letters*, *45*(19), 10482–10492. https://doi.org/10.1029/2018GL078758

Ding, L., & Farmer, D. M. (1994). Observations of breaking surface wave statistics. *Journal of Physical Oceanography*, *24*(6), 1368–1387. https://doi.org/10.1175/1520-0485(1994)024⟨1368:oobsws⟩2.0.co;2

Drazen, D. A., Melville, W. K., & Lenain, L. (2008). Inertial scaling of dissipation in unsteady breaking waves. *Journal of Fluid Mechanics*, *611*, 307–332. https://doi.org/10.1017/S0022112008002826

Duncan, J. H. (1981). Experimental investigation of breaking waves produced by a towed hydrofoil. *Proceedings of The Royal Society of London, Series A: Mathematical and Physical Sciences*, *377*(1770), 331–348. https://doi.org/10.1098/rspa.1981.0127

Frouin, R., Schwindling, M., & Deschamps, P. Y. (1996). Spectral reflectance of sea foam in the visible and near-infrared: In situ measurements and remote sensing implications. *Journal of Geophysical Research*, *101*(C6), 14361–14371. https://doi.org/10.1029/96JC00629

Henry, C. L. (2009). *Bubbles, thin films and ion specificity* (p. 220). Thesis(January).

Kleiss, J. M., & Melville, W. K. (2010). Observations of wave breaking kinematics in fetch-limited seas. *Journal of Physical Oceanography*, *40*(12), 2575–2604. https://doi.org/10.1175/2010JPO4383.1

Kleiss, J. M., & Melville, W. K. (2011). The analysis of sea surface imagery for whitecap kinematics. *Journal of Atmospheric and Oceanic Technology*, *28*(2), 219–243. https://doi.org/10.1175/2010JTECHO744.1

Koepke, P. (1984). Effective reflectance of oceanic whitecaps. *Applied Optics*, *23*(11), 1816. https://doi.org/10.1364/ao.23.001816

Korinenko, A. E., Malinovsky, V. V., Kudryavtsev, V. N., & Dulov, V. A. (2020). Statistical characteristics of wave breakings and their relation with the wind waves' energy dissipation based on the field measurements. *Physical Oceanography*, *27*(5), 472–488. https://doi.org/10.22449/1573-160X-2020-5-472-488

Kubryakov, A. A., Kudryavtsev, V. N., & Stanichny, S. V. (2021). Application of Landsat imagery for the investigation of wave breaking. *Remote Sensing of Environment*, *253*, 112144. https://doi.org/10.1016/j.rse.2020.112144

Lamarre, E., & Melville, W. K. (1991). Air entrainment and dissipation in breaking waves. *Nature*, *351*(No. 6326), 469–472. https://doi.org/10.1038/351469a0

Lenain, L., Pizzo, N., & Melville, W. K. (2019). Laboratory studies of Lagrangian transport by breaking surface waves. *Journal of Fluid Mechanics*, *876*, 1–12. https://doi.org/10.1017/jfm.2019.544

Malila, M. P., Thomson, J., Breivik, Ø., Benetazzo, A., Scanlon, B., & Ward, B. (2022). On the groupiness and intermittency of oceanic whitecaps. *Journal of Geophysical Research: Oceans*, *127*(1). https://doi.org/10.1029/2021JC017938

Masnadi, N., Chickadel, C. C., & Jessup, A. T. (2021). On the thermal signature of the residual foam in breaking waves. *Journal of Geophysical Research: Oceans*, *126*(1). https://doi.org/10.1029/2020JC016511

Melville, W. K. (1996). The role of surface-wave breaking in air-sea interaction. *Annual Review of Fluid Mechanics*, *28*(1), 279–321. https://doi.org/10.1146/annurev.fl.28.010196.001431

Melville, W. K., & Matusov, P. (2002). Distribution of breaking waves at the ocean surface. *Nature*, *417*(6884), 58–63. https://doi.org/10.1038/417058a

Monahan, E. C. (1971). Oceanic whitecaps. *Oceanic Whitecaps*, *1*(No. 2), 139–144. https://doi.org/10.1175/1520-0485(1971)001⟨0139:ow⟩2.0.co;2

Monahan, E. C., & O'muircheartaigh, I. G. (1986). Whitecaps and the passive remote sensing of the ocean surface. *International Journal of Remote Sensing*, *7*(5), 627–642. https://doi.org/10.1080/01431168608954716

Phillips, O. M. (1985). Spectral and statistical properties of the equilibrium range in wind-generated gravity waves. *Journal of Fluid Mechanics*, *156*(-1), 505–531. https://doi.org/10.1017/S0022112085002221

Phillips, O. M., Posner, F. L., & Hansen, J. P. (2001). High range resolution radar measurements of the speed distribution of breaking events in wind-generated ocean waves: Surface impulse and wave energy dissipation rates. *Journal of Physical Oceanography*, *31*(2), 450–460. https://doi.org/10.1175/1520-0485(2001)031⟨0450:HRRRMO⟩2.0.CO;2

Rapp, R. J., & Melville, W. K. (1990). Laboratory measurements of deep-water breaking waves. *Philosophical Transactions of the Royal Society of London - Series A: Mathematical and Physical Sciences*, *331*(1622), 735–800. https://doi.org/10.1098/rsta.1990.0098

Romero, L. (2019). Distribution of surface wave breaking fronts. *Geophysical Research Letters*, *46*(17–18), 10463–10474. https://doi.org/10.1029/2019GL083408

Scanlon, B., & Ward, B. (2016). The influence of environmental parameters on active and maturing oceanic whitecaps. *Journal of Geophysical Research: Oceans*, *121*(5), 3325–3336. https://doi.org/10.1002/2015JC011230

Schwendeman, M., Thomson, J., & Gemmrich, J. R. (2014). Wave breaking dissipation in a young wind sea. *Journal of Physical Oceanography*, *44*(1), 104–127. https://doi.org/10.1175/JPO-D-12-0237.1

Sinnis, J. T., Grare, L., Lenain, L., & Pizzo, N. (2021). Laboratory studies of the role of bandwidth in surface transport and energy dissipation of deep-water breaking waves. *Journal of Fluid Mechanics*, *927*, 1–23. https://doi.org/10.1017/jfm.2021.734

Strand, K. O., Breivik, Ø., Pedersen, G., Vikebø, F. B., Sundby, S., & Christensen, K. H. (2020). Long-term statistics of observed bubble depth versus modeled wave dissipation. *Journal of Geophysical Research: Oceans*, *125*(2), 1–14. https://doi.org/10.1029/2019JC015906

Stringari, C., Veras Guimarães, P., Filipot, J.-F., Leckler, F., & Duarte, R. (2021). Deep neural networks for active wave breaking classification. *Scientific Reports*, *11*(1), 3604. https://doi.org/10.1038/s41598-021-83188-y

Sutherland, P., & Melville, W. (2015). Field measurements of surface and near-surface turbulence in the presence of breaking waves. *Journal of Physical Oceanography*, *45*(4), 943–965. https://doi.org/10.1175/JPO-D-14-0133.1

Sutherland, P., & Melville, W. K. (2013). Field measurements and scaling of ocean surface wave-breaking statistics. *Geophysical Research Letters*, *40*(12), 3074–3079. https://doi.org/10.1002/grl.50584

Tian, Z., Perlin, M., & Choi, W. (2010). Energy dissipation in two-dimensional unsteady plunging breakers and an eddy viscosity model. *Journal of Fluid Mechanics*, *655*, 217–257. https://doi.org/10.1017/S0022112010000832

Wurl, O., Miller, L., Johnson, K., & Vagle, S. (2011). Formation and global distribution of sea-surface microlayers. *Biogeosciences*, *8*(1), 121–135. https://doi.org/10.5194/bg-8-121-2011

Zappa, C. J., Banner, M. L., Morison, R. P., & Brumer, S. E. (2016). On the variation of the effective breaking strength in oceanic sea states. *Journal of Physical Oceanography*, *46*(7), 2049–2061. https://doi.org/10.1175/JPO-D-15-0227.1

Zou, X., Babanin, A. V., Schulz, E. W., Manasseh, R., & Guan, C. (2022). Passive acoustic determination of spectral wave breaking dissipation. *Journal of Physical Oceanography*, *52*(11), 2807–2823. https://doi.org/10.1175/JPO-D-21-0307.1